

New State of the Arctic Ocean's Beaufort Gyre

Peigen Lin (✉ plinwhoi@gmail.com)

Woods Hole Oceanographic Institution <https://orcid.org/0000-0002-2410-976X>

Robert Pickart

Woods Hole Oceanographic Institution <https://orcid.org/0000-0002-7826-911X>

Harry Heorton

Centre for Polar Observation and Modelling, University College London <https://orcid.org/0000-0003-0447-7028>

Michel Tsamados

Centre for Polar Observation and Modelling

Motoyo Itoh

Japan Agency for Marine-Earth Science and Technology

Takashi Kikuchi

Japan Agency for Marine-Earth Science and Technology

Article

Keywords:

Posted Date: August 26th, 2022

DOI: <https://doi.org/10.21203/rs.3.rs-1774491/v1>

License: © ⓘ This work is licensed under a Creative Commons Attribution 4.0 International License.

[Read Full License](#)

New State of the Arctic Ocean's Beaufort Gyre

Peigen Lin¹, Robert S. Pickart¹,
Harry Heorton², Michel Tsamados²,
Motoyo Itoh³, Takashi Kikuchi³

1. Woods Hole Oceanographic Institution, USA

2. Department of Earth Sciences, University College London, UK

3. Institute of Arctic Climate and Environment Research, Japan Agency for Marine-Earth
Science and Technology, Yokosuka, Japan

Submitted to *Nature Geoscience*

June 2022

Corresponding Author: Peigen Lin (plinwhoi@gmail.com)

Abstract

The anti-cyclonic Beaufort Gyre is the dominant circulation of the Canada Basin and the largest freshwater reservoir in the Arctic Ocean. Using an extensive historical hydrographic dataset together with updated satellite dynamic ocean topography data, we find that the Beaufort Gyre has transitioned to a new state in which the increase in sea surface height of the gyre has slowed and the freshwater content has stabilized. In addition, the cold halocline layer has thinned significantly due to less input of cold and salty water stemming from the Pacific Ocean and the Chukchi Sea shelf, together with greater entrainment of lighter water from the eastern Beaufort Sea. The new state of the Beaufort Gyre is due to a southwestward shift in its location as a result of variation in the regional wind forcing. Our results imply that continued thinning of the cold halocline layer could disrupt the present stable state, allowing for a significant freshwater release. This in turn could freshen the subpolar North Atlantic, impacting the Atlantic Meridional Overturning Circulation.

The Beaufort Gyre is the largest freshwater reservoir in the Arctic Ocean¹⁻³. It is driven by the anti-cyclonic winds in the Canada Basin, which historically have waxed and waned on interannual timescales in conjunction with the Arctic Oscillation⁴. However, since 2000 the Arctic Oscillation has remained predominantly negative, and, as a result, the Beaufort Gyre has strengthened and its freshwater content has increased by 40% relative to the 1970's climatology⁵. Associated with the accumulating freshwater, the gyre has expanded northwestward, with its center approaching the vicinity of the Chukchi Plateau^{6,7}. At the same time the layer of cold Pacific-origin water in the gyre has widened laterally and thickened vertically⁸. There are many potential impacts of the changing Beaufort Gyre on the hydrographic structure, physical processes, and ecosystem of the Arctic, both local and remote. As such, it is of high interest to better understand the factors associated with such changes – including the underlying causes.

The gyre strength generally coincides with the intensity of the surface forcing, and its lateral extent is affected by the location of the atmospheric Beaufort High^{3,9}. In the presence of sea ice, the surface forcing is a combination of the wind stress and the ice-ocean stress^{10,11}. As the gyre spins up, the acceleration of the geostrophic circulation reduces the ice-ocean stress which in turn weakens the forcing. This mechanism of Beaufort Gyre stabilization has been referred to as the ice-ocean governor¹². Another negative feedback to the strengthening of the gyre is that the growing freshwater content and bowing halocline generate more eddies via baroclinic instability, which in turn dampen the gyre and flatten the halocline¹³⁻¹⁵. Both modeling and satellite sea surface height measurements have suggested that the Beaufort Gyre stabilized from 2008 to 2014^{16,17}. However, it is unknown if this is represented an overall change in the state of the gyre, nor have the underlying reasons for any such change been addressed observationally.

A major source of the interannual variation in freshwater content of the gyre is the Pacific-origin water entering through Bering Strait⁵. A substantial portion of this water is subsequently fluxed off the Chukchi shelf through Barrow Canyon, particularly during summer¹⁸, and is ultimately injected into the Beaufort Gyre via boundary currents and cross-stream processes¹⁹⁻²². River runoff, particularly from the Mackenzie River, is believed to contribute nearly equally to the interannual variation, while sea ice melt and net precipitation are thought to impact the seasonality more^{5,23}.

If and when the Beaufort Gyre finally relaxes, the unprecedented amount of freshwater stored in the gyre will start to release. This in turn could lead to a substantial flux of freshwater to the North Atlantic, which could potentially freshen the upper limb of the Atlantic Meridional Overturning Circulation, a key component of the global climate^{24,25}. A recent model study estimated that the 40% excess freshwater presently stored in the gyre could freshen the western shelves of the Labrador Sea by 0.4 ²⁶. If this freshwater then spreads into the North Atlantic subpolar gyre, this could significantly reduce the convective activity, as happened during the Great Salinity Anomaly²⁷.

Our study investigates the long-term trends of the Beaufort Gyre and reveals that it has attained a new state over the last decade. We use an extensive updated collection of historical hydrographic data and satellite dynamic ocean topography data to characterize this state and provide insights into the reasons for the change. We quantify the evolution of the gyre in terms of its sea surface height and freshwater content, and explore the connection to the cold halocline layer. As the gyre has evolved to its new state the halocline has thinned considerably, the causes of which are addressed.

Long-term trend of the Beaufort Gyre

The state of Beaufort Gyre (BG) is reflected by the dynamic ocean topography (DOT) averaged over the BG region (Fig. 1a). The newly-updated DOT data presented here extend the timeseries to 2019, allowing us to further address the DOT changes in recent years and to assess the trends over a longer time period. The spatially averaged DOT of the BG generally increased from 2003-2019 (Fig. 1b), but there are notable variations around this trend. We divide the record into two time periods: from 2003-2011 and 2012-2019. In the first period there was a strong increase in the average DOT throughout the BG region, with a maximum trend of 0.035 m yr⁻¹ in the northwest Canada Basin where the gyre expanded to (Fig. 2a). This is consistent with a previous result⁷. Since that time the BG has continued to strengthen, but has done so at a considerably slower rate (with a short weakening from 2011-2013, Fig. 1b). Unlike the earlier period, the increase in DOT occurred predominantly in the southeast part of the Canada Basin (Fig. 2c). Meanwhile, a decreasing trend is found west of the Chukchi Plateau with a maximum

value of -0.022 m yr^{-1} . These changes indicate that, over the last decade, the BG has contracted and shifted to the southeast part of the basin.

To illustrate how the freshwater content (FWC) has varied in relation to the changes in the strength of the BG, we calculated the annual mean FWC using the historical hydrographic data (Fig. 1c). The FWC was approximately $16,000 \text{ km}^3$ in 2003 and grew to over $22,000 \text{ km}^3$ in 2011, consistent with previous observational estimates¹. This corresponds to a trend of $940 \text{ km}^3 \text{ yr}^{-1}$. However, the situation changed dramatically in the second period during which time the FWC underwent large fluctuations, ranging between $22,000$ and $24,000 \text{ km}^3$. During this time the trend is still slightly positive, but not statistically significant. We also constructed a timeseries of FWC using the DOT data together with estimates of the ocean mass from GRACE (see Methods). These two FWC estimates are in phase with each other and have comparable trends. Such good agreement of the two independent datasets drives home the fact that the BG has entered a new regime whereby the increase of the DOT has slowed and the FWC has plateaued.

Thinning of Cold Halocline Layer

We now investigate the response of the water column in the BG region during the second period. Below the surface mixed layer, the halocline acts as a barrier to the warm underlying Atlantic water, shielding the major portion of the freshwater content in the gyre¹. The halocline in the western Arctic generally consists of the warm halocline originating from the Pacific summer water^{4,22}, sitting atop the cold halocline which is ventilated by the Pacific winter water together with the cold and salty water formed/modified locally on the shelves of the Chukchi and Beaufort Seas via brine rejection²⁸⁻³⁰. The warm halocline layer corresponds to a salinity (S) range of 28 to 32.6, while the cold halocline layer (CHL) spans the range 32.6 to 33.9. These were identified using mean vertical profiles within the BG (see Methods).

We computed trends in the volume of water within salinity classes spanning both the warm and cold haloclines in the BG region for the two periods considered above: 2003-2011 and 2012-2019 (Fig. 3). (We are unable to quantify the trends for layers with $S < 28$ due to the limitation of the data near the surface.) In the first period the trends are positive for $S > 30$, particularly in the CHL. The thickening halocline coincides with the doming DOT in the early period (Fig. 1a). By

contrast, the trends are significantly negative in the CHL in the later period, peaking at $-600 \text{ km}^3 \text{ yr}^{-1}$ for waters with $S \sim 33$, while the trends remain relatively close to zero at shallower depths. This suggests that the thinning of the CHL results in the thinning of the entire halocline. One might then ask, what is the impact of changes in the width of the CHL on the layer thickness of the entire freshwater reservoir lying above the Atlantic water?

To address this we constructed thickness anomaly timeseries, relative to the value in 2003, for (1) the CHL layer; (2) the layer from the surface to the top of the CHL (comprised of the warm halocline and the surface mixed layer); and (3) the sum of these two; i.e., the full layer above the underlying Atlantic water (Fig. 1d). Associated with the changes of DOT and FWC, the full layer thickened markedly by 5.8 m yr^{-1} in the early period, due mostly to thickening of the layer above the CHL, although the CHL did undergo a net expansion during this period. By contrast, since 2012 the CHL has been thinning at a rate of -1.5 m yr^{-1} , offsetting the expansion of the upper layer and causing a 90% reduction of the thickening rate of the total layer. This trend in the width of the CHL has not been spatially uniform, however (Fig. 2e): while thinning has occurred over a large portion of the BG region, particularly west of the Chukchi Plateau, the layer has thickened in the southeast portion of the Canada Basin. This agrees well with the spatial trends of DOT and FWC during the second period (Fig. 2c,d). These results imply that the thinning of the CHL has played a dominant role in the stabilization of the thickness of the water column above the Atlantic layer in recent years, as well as significantly affecting the variations of the FWC and DOT.

It has been argued that the relocation and expansion of the BG during the early period was caused primarily by the strengthening atmospheric Beaufort High and its enhanced negative wind stress curl^{7,9}, although other factors, e.g., ice drift and eddy activity, are not negligible. To further investigate the role of atmospheric forcing during the second period, we constructed a map of the trend of wind stress curl from 2012-2019 (Fig. 2f). A negative trend of wind stress curl is evident in the southeast part of the Canada basin where the DOT and FWC increased. This makes sense dynamically in that enhanced negative wind stress curl leads to stronger Ekman pumping, which in turn domes the DOT and accumulates more freshwater regionally. At the same time, the decrease of DOT and FWC to the west of the Chukchi Plateau is likely associated with the

positive trend of wind stress curl in this region. This highlights the importance of the position and extent of the BG, which in turn is related to the location of the atmospheric Beaufort High.

Causes of the thinning CHL

Pacific-origin winter water is the main source water that ventilates the CHL in the western Arctic Ocean^{8,30}. Concomitant with the increased Bering Strait inflow, the Pacific water has become markedly warmer and fresher. These changes suggest that the Pacific winter water which previously ventilated the CHL in the 1990s likely now more readily affects the shallower layer in the basin³¹. This is in line with our results of the thinning CHL and the thickening of the layer immediately above (Fig. 3). However, as the Pacific winter water transits across the Chukchi shelf with a residence time of 4.5-7.5 months³², its salinity can be increased before reaching the basin via brine rejection during ice formation^{28,33,34}. Hence, it is unclear how these offsetting effects have been playing out. Since Barrow Canyon is a choke point through which a significant portion of Pacific-origin water flows into the basin, we now use mooring data at the mouth of the canyon to further elucidate the source water that eventually impacts the CHL in the BG region.

Fig. 3 shows the trends of the volume of water fluxed off the shelf through Barrow Canyon in each salinity class through the water column. One sees that in both periods the trends of the Barrow Canyon outflow are in line with the volume trends in the basin computed above; in particular, positive trends from 2003-2011, peaking above the CHL layer, and negative trends from 2012-2019, with the maximum near a salinity of 33 in the CHL. Note, however, that the trends of the Barrow Canyon outflow water that supplies the CHL are less than the ones in the basin (although they are not significantly different), and the discrepancy is greater in the later years. These results thus indicate two important aspects regarding ventilation in the basin: the Barrow Canyon outflow water cannot solely explain the total trend of the CHL in the BG, and the contribution from the canyon is reduced in the later years.

Cold and salty winter water is also regularly formed along the eastern Beaufort Sea shelf and fluxed offshore by downwelling²⁹. It has been previously emphasized that the contribution of freshwater from the eastern Beaufort Sea is comparable to the Pacific-origin water⁵. It is thus reasonable to consider the locally-formed winter water in the eastern Beaufort Sea as the other

important source water of the CHL in the BG. It is worth noting that the Barrow Canyon outflow can feed the eastern Beaufort Sea via the eastward-flowing Beaufort shelfbreak jet³⁵. However, the jet is centered near the 150 m isobath and is bottom-intensified in the mean, particularly in the cold months³⁶, and thus it has a minor impact on the winter water on the shelf.

To investigate the impact of the eastern source of winter water, we conducted Lagrangian tracer experiments based on the annual mean velocity field averaged over the CHL from the GLORYS12 ocean reanalysis product (the GLORYS12 velocities show good agreement with observations³⁷). The first experiment was done for the extreme year of 2011, at the end of the early period, when the DOT core of the BG was located at its westernmost location during this period (Fig. 4a). Passive tracers denoted by blue and red colors were released along the 100 m isobath in the Chukchi Sea/western Beaufort Sea (CS/WBS) and eastern Beaufort Sea (EBS), respectively (Fig. 4b). After one year, most of the CS/WBS tracer progressed into the BG region near the Chukchi Plateau. The majority of these parcels emanated from the eastern side of Barrow Canyon and subsequently turned to the west, consistent with previous observational and modeling studies^{20,38-40}. By contrast, most of the EBS tracer stayed very close to the location where it was released. To quantify this, we computed the percentage of the CS/WBS and EBS tracer that resided for more than half the year in the BG region (within the purple polygon in Fig. 1a). This revealed that 90% of the CS/WBS tracer did so, compared to only 15% for the EBS tracer.

A second experiment was then conducted for the year 2019, when the DOT core of the BG had shifted to the southeast part of the basin (Fig. 4a). In this case, 84% of the CS/WBS tracer progressed into the BG region near the Chukchi Plateau, slightly less than the first experiment. However, the percentage of EBS tracer reaching this region increased dramatically to 73%. This suggests that the contribution of the EBS water to the CHL is dynamically linked to the BG state: when the gyre shifts to the southeast, the CHL is more likely to be significantly ventilated by winter water emanating from the eastern Beaufort Sea shelf.

The question remains as to the role of the EBS water in the thinning of the CHL. To address this, we used the historical hydrographic data and computed the fractional occurrence of the water in each of the salinity classes of Fig. 3 on the EBS shelf and on the CS/WBS shelf (extending southward to 70.5°N for the latter). This revealed that, for the warm halocline layer, the

fractional occurrence was similar for the two regions, while for the CHL the fractional occurrence was larger on the CS/WBS shelf. This, together with the fact that the area of the CS/WBS shelf is greater than that of the EBS, implies that the potential source volume of cold halocline water is larger on the CS/WBS shelf. Hence, during the second period when there is enhanced influence from the EBS (Fig. 4c), the amount of available shelf water in the salinity class of the CHL is less, implying that the CHL would thin. We conclude then that both the reduced Barrow Canyon outflow and the southeast shift in the BG location led to the reverse in trend of the CHL thickness from the early to the late period.

Discussion

Our results have demonstrated that, during the last decade, the BG has transitioned to a new state, shifting towards the southeast Canada Basin where the negative wind stress curl has intensified, together with a dampened rate of increase of sea surface height, stabilization of freshwater content, and thinning of the CHL. The recent decrease in the amount of Pacific-origin winter water exiting Barrow Canyon explains some of the CHL thinning, while the enhanced influence from the eastern Beaufort Sea – due to the southeastward shift of the BG – likely contributes as well.

Previous work has demonstrated that the local wind patterns modulating the BG are related to the large-scale Arctic Oscillation (AO)^{4,41}. On interannual timescales, positive AO states are associated with a contracted BG situated in the southeast Canada Basin, while negative AO states correspond to an expanded BG. A similar relationship holds on decadal timescales, with a northwestward expansion and movement during 2003-2011 when the AO index was mostly negative, and southeastward shift during 2012-2019 when the AO was mainly in the positive state (Extended Data Fig. 1). We emphasize, however, that the new state of the BG documented here does not represent a return to the initial condition of 2003 when the gyre was weak and located partially in the southeastern basin. Instead, the gyre has continuously intensified even though it has contracted (Fig. 4a), and it has maintained its excess freshwater storage. That said, with a continued thinning of the CHL due to a decrease in the source winter water, the DOT of the gyre may eventually drop, disrupting the present stable state and allowing a significant freshwater

release. This in turn could freshen the subpolar North Atlantic, impacting the Atlantic Meridional Overturning Circulation.

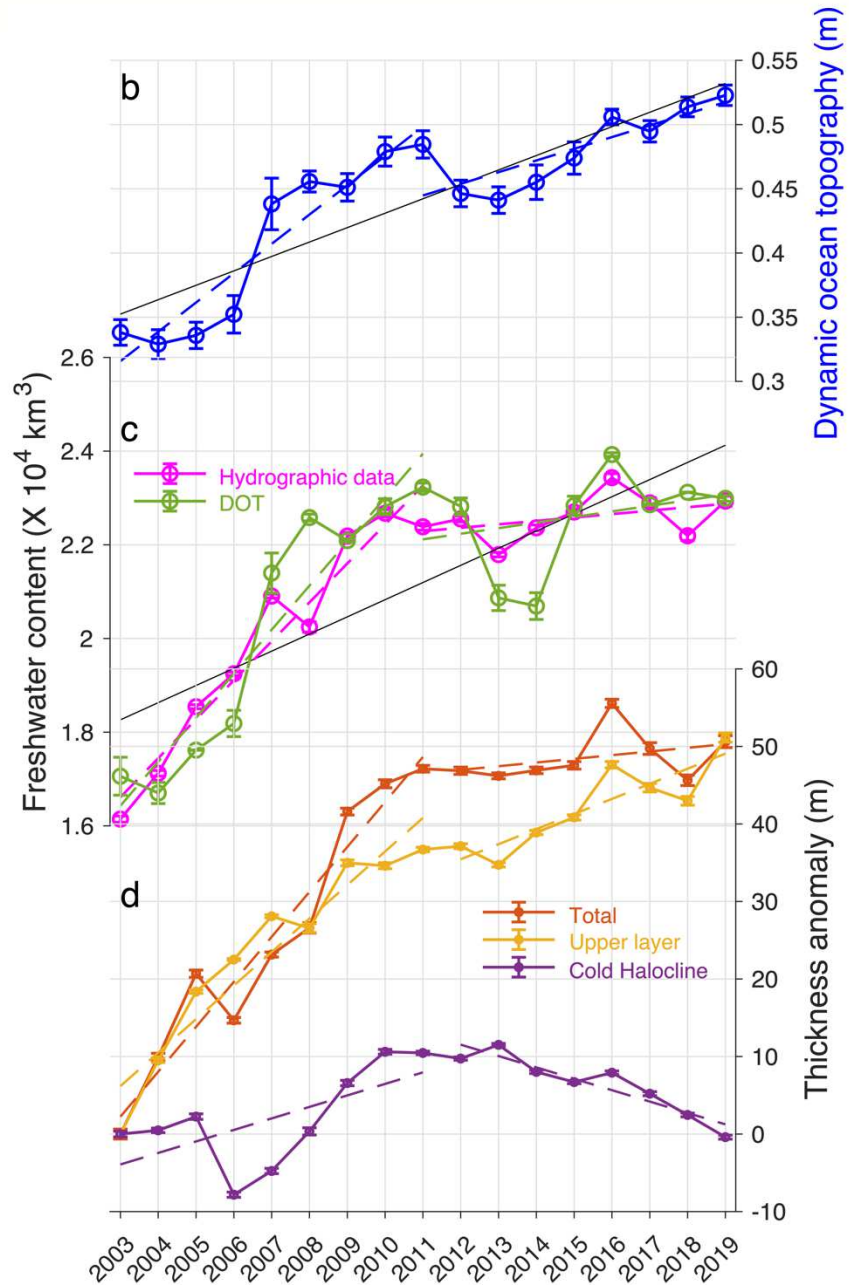
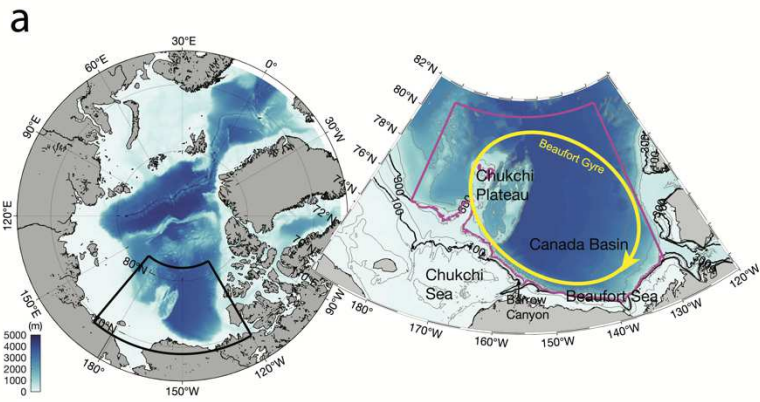


Fig. 1 | Long-term trends of the Beaufort Gyre: 2003-2011 versus 2012-2019. **a**, Geographic map of the Arctic Ocean with an enlarged view of the study region. The schematic Beaufort Gyre is marked by the yellow circle. The Beaufort Gyre region is delimited by the thick purple line, over which area averages are computed, shown in b-d. The bathymetry is from IBCAO v3. **b**, The annual mean ocean dynamic topography (m); **c**, The annual mean freshwater content ($\times 10^4 \text{ km}^3$) estimated using the dynamic ocean topography and GRACE data (green), and using the historical hydrographic data (magenta); **d**, The annual mean thickness anomalies (m) relative to 2003 of the layer from the surface to the top of the cold halocline (yellow), the cold halocline layer beneath this (purple), and the sum of the two layers (orange). The standard errors are included. The dashed lines are the linear trends in the early and late periods, and the black lines in b and c denote the linear trends over the full study period.

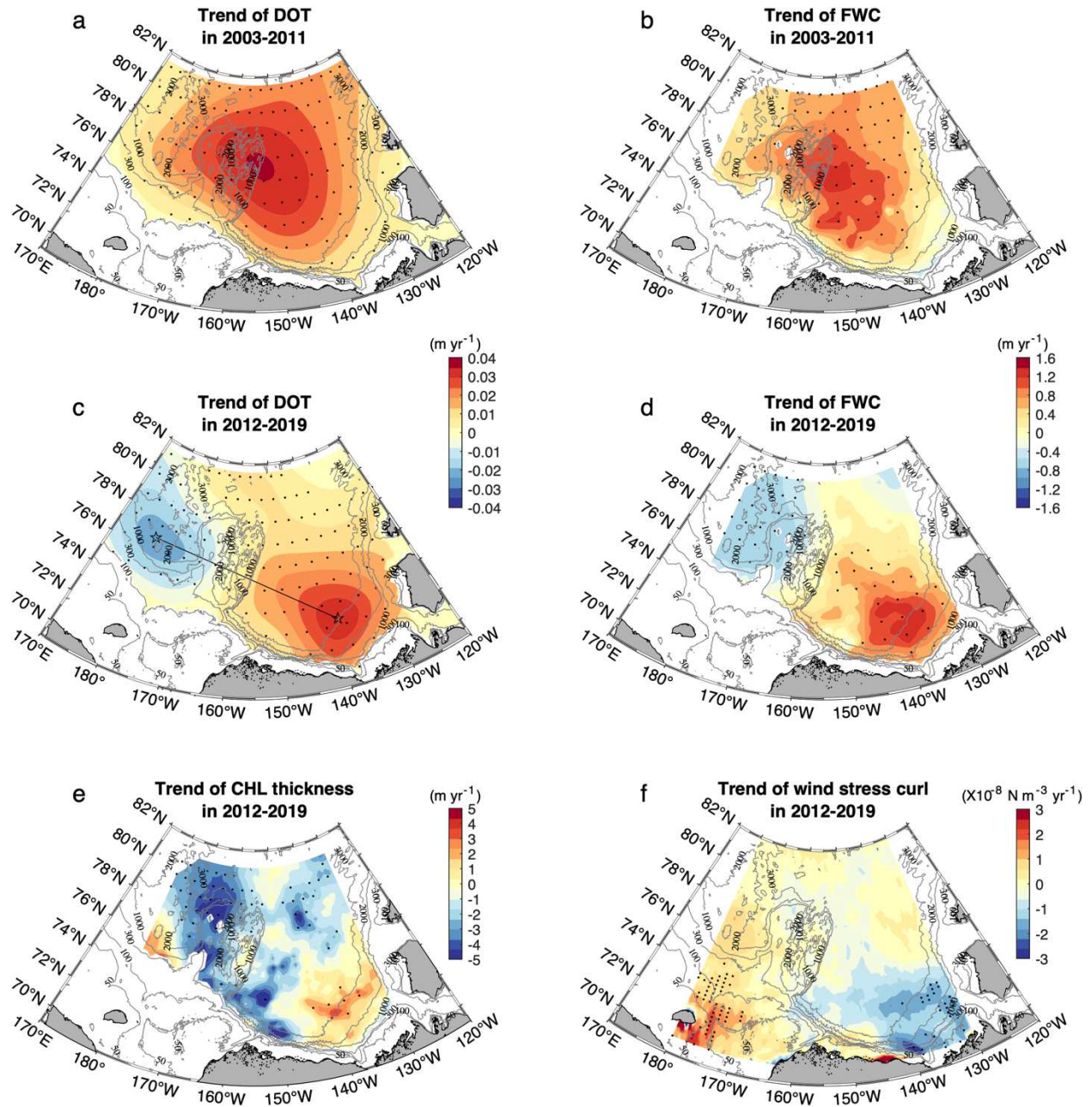


Fig. 2 | Spatial distribution of the trends in the Beaufort Gyre. **a,c**, Trends of dynamic ocean topography in the early period (2003-2011) and in the late period (2012-2019); **b,d**, trends of the freshwater content in the early period and in the late period; **e,f**, trends of the thickness of the cold halocline layer and the wind stress curl in the late period. The dots (which are subsampled) represent the areas with statistically significant trends. The line connecting the two centers of the trends in c is used to construct the Hovmöller plot in Fig. 4a.

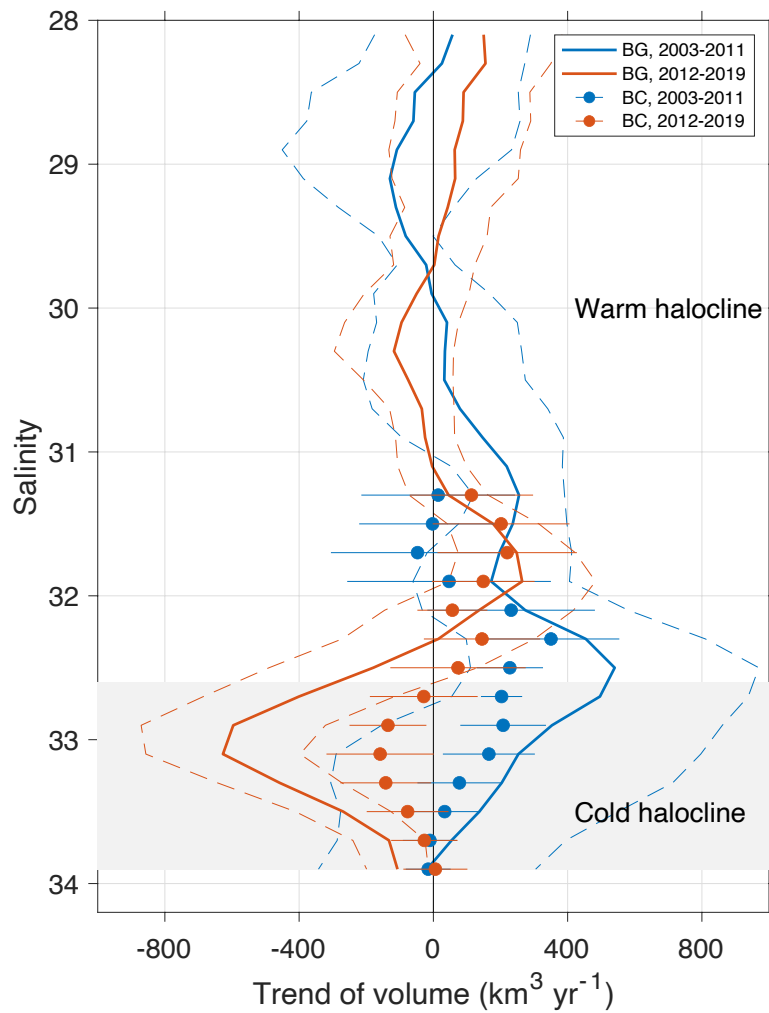


Fig. 3 | Linear trends of volume within salinity classes in relation to the source water. Trends of volume in the Beaufort Gyre region (curves) and in the main source water at the mouth of Barrow Canyon (filled circles), in the early period (2003-2011, blue) and the late period (2012-2019, red). The standard errors are denoted by the dashed lines and horizontal bars. The shaded region is the cold halocline layer.

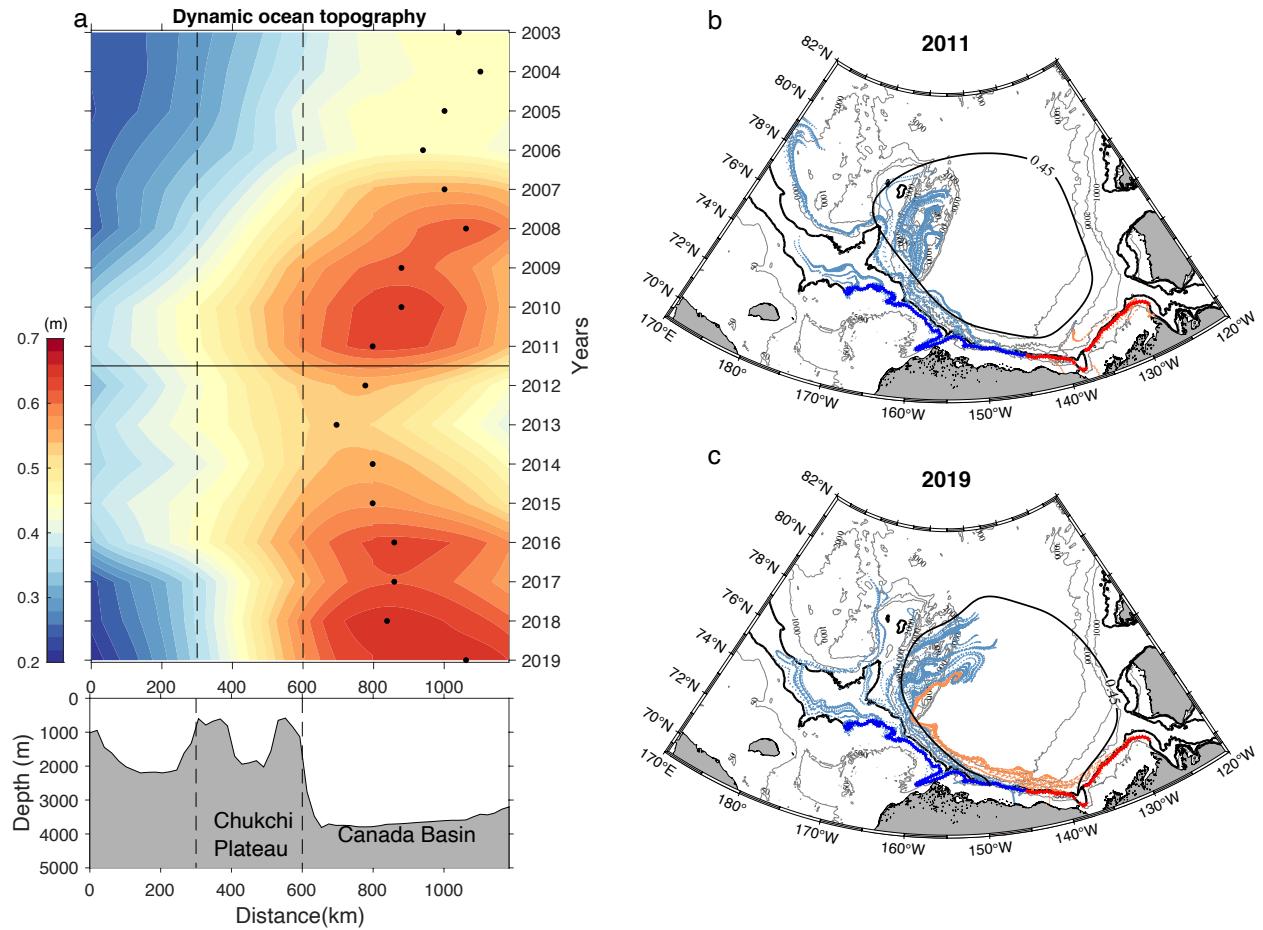


Fig. 4 | Inferred contributions to the cold halocline layer (CHL) in the Beaufort Gyre region. a, Hovmöller diagram of dynamic ocean topography (DOT, m) along the line in Fig. 2c from 2003 to 2019 (upper panel), with the dots denoting the maximum DOT in each year, and the horizontal solid line separating the two time periods. The associated bathymetry is shown (bottom panel), where the east and west edges of the Chukchi Plateau are denoted by the vertical dashed lines. **b,** The passive tracer experiment in 2011. The 0.45 m DOT contour representing the location of the Beaufort Gyre is shown (black curve). The tracer is released along the 100 m isobath in the Chukchi Sea/western Beaufort Sea (CS/WBS, blue dots) and in the eastern Beaufort Sea (EBS, red dots). The trajectories of the tracer particles after one year are colored light blue for the CS/WBS and light red for the EBS. **c,** same as **b** except for the experiment in 2019.

Acknowledgements

Funding for the study was provided by National Science Foundation grant OPP-1733564 and National Oceanic and Atmospheric Administration grant NA19OAR4320074 (P.L., R.S.P.), Arctic Challenge for Sustainability projects (ArCS and ArCSII) of the Ministry of Education, Culture, Sports, Science and Technology (M.I., T.K.)

Author contributions

P.L. led the data analysis and results interpretation, with assistance from all co-authors. P.L. and R.S.P. wrote the manuscript with input from all co-authors. H.H. and M.T. produced the updated dynamic ocean topography data from 2011-2019. M.I. and T.K. provided the long-term data from the mooring array at the mouth of Barrow Canyon.

Methods

Historical hydrographic data. We have assembled an extensive historical hydrographic dataset that consists of temperature and salinity profiles measured by ships, expendable probes, ice-tethered profilers, and gliders, from four sources: (a) the World Ocean Database 2018 (WOD18), obtained from the National Centers for Environmental Information, spanning from 1849-2020 in the Arctic Ocean; (b) the Unified Database for Arctic and Subarctic Hydrography (UDASH), which is a composite dataset of salinity and temperature profiles in the domain north of 65°N covering 1980-2015⁴²; (c) a collection of hydrographic data from the Chukchi Sea from various international sources, spanning 1922-2019⁴³; and (d) additional hydrographic profiles in the Beaufort Gyre from the Arctic Data Center and the Beaufort Gyre Exploration Project¹. We removed duplicate profiles. In this study we focus on the data from 2003 to 2019 (Extended Data Fig. 2).

While the datasets above have been previously scrutinized, further quality control and error checking were applied as described in Lin et al.²¹. To construct lateral maps of the variables we grid the data using a Laplacian-spline interpolation scheme⁴⁴ with a grid spacing of 1° in longitude and 0.25° in latitude. Further gridding was done for salinity bins, spanning the range 28-34 with an interval of 0.2, and trends were computed using this gridded product.

Dynamic ocean topography.

We employ the monthly altimetry-derived dynamic ocean topography (DOT, sea surface height referenced to the geoid) product from 2003-2014, with a resolution of $0.75^\circ \times 0.25^\circ$ ⁴⁵. Following the previous methodology, we extended the time series using the original processing algorithm for the full CryoSat2 time series and up to 88°N . The algorithm is described briefly here, with the reader directed to Armitage et al.⁴⁵ for the full technical description. Satellite open ocean surface elevations were obtained from the Low Resolution (LRM) and SAR ocean modes, and from leads (cracks in the sea ice cover) from SAR Ice and SAR Interferometric modes. The UCL13 Mean Sea Surface product was used to calculate the Sea Level Anomaly (SLA) for all four modes. A monthly mean SLA offset of LRM to SAR ocean, SAR ocean to SAR lead, SAR lead to SARIN lead, from coincident measurements on a 100-km resolution grid was calculated to remove mode bias compared to the LRM mode SLA. Following this, the GOCO03s geoid was used to calculate the DOT, removing the bias from the sea level anomaly calculation. The individual DOT and SLA measurements were collected onto the $0.75^\circ \times 0.25^\circ$ grid with outliers above and below the 10th percentiles removed. A smoothed DOT using a 100 km Gaussian kernel was created with the gradient taken to give geostrophic surface currents. Following the repeat usage of the Armitage et al. algorithm⁴⁵, differences between the original and updated datasets over the period 2011-2014, are less than 1%.

Moorings. Japan Agency for Marine-Earth Science and Technology (JAMSTEC) has maintained three moorings across the mouth of Barrow Canyon (Extended Data Fig. 2) since 2001, except for the four years of Jun 2004 – Sep 2005, Sep 2008 – Aug 2010, and Oct 2013 – Aug 2014¹⁸. The middle mooring is situated in the center of Barrow Canyon (BCC), and the other two moorings are on the eastern and western flanks (BCE and BCW, respectively). All three moorings were equipped with MicroCATs for measuring hourly temperature and salinity, and Acoustic Doppler Current Profilers (ADCPs) or point current meters for measuring velocities every 0.25-2 hours. The ADCP velocity profiles have bin sizes between 4-8 m. The accuracies of the sensors are 0.001°C for temperature, 0.01 for salinity, and 0.01 m s^{-1} for velocity²⁸. The temperature, salinity

and velocity are gridded along the section across the mouth of Barrow Canyon, with a grid size of 2 km in the horizontal and 2 m in the vertical. Due to the lack of data in the upper 50 m, the gridded vertical sections only cover the portion of the water column deeper than salinity = 31. The volume of water fluxed across the section in each year is calculated by the mean velocity, cross sectional area, and time. In this study, we use the data from 2003 to 2019, consistent with the DOT data.

Reanalysis data. We compute wind stress curl using the hourly wind data from the ERA5 reanalysis, provided by the European Center for Medium-Range Weather Forecasts (ECMWF⁴⁶). The ERA5 is the fifth generation ECMWF reanalysis product with a grid spacing of $0.25^\circ \times 0.25^\circ$. It has been widely used in previous high-latitude studies^{21,47}.

The Lagrangian tracer experiments carried out in the study make use of the velocity data in the cold halocline layer from the global eddy-resolving physical ocean and sea ice reanalysis (GLORYS12³⁷), obtained from the Copernicus Marine and Environment Monitoring Service (CMEMS). GLORYS12 is a NEMO-based reanalysis that assimilates satellite observations and historical hydrographic profiles. It has a horizontal resolution of $1/12^\circ$, and 50 vertical levels with increased resolution in the upper layer (1-30 m interval in the upper 200 m).

GRACE. We use the monthly equivalent water thickness from the GRACE/GRACE-FO Mascon solutions (release-06, version 2) from the Center for Space Research (CSR⁴⁸) to estimate the freshwater content (see below). There are 31 months of gaps in the two-decade record due to the satellite's regular battery management. To fill each of the gaps, we apply a 5-month weighting window centered at the month in question⁴⁵. This technique was not applicable for 2017-2018 when there were successive gap months. In this case, we filled each gap with the mean of the same month from the year before and after. The GRACE data have a spatial resolution of 0.25° , and were interpolated onto the same grid as the DOT data.

Vertical structure of the water column. The different vertical layers considered in the study are depicted in Extended Data Fig. 3 using mean hydrographic profiles from the Beaufort Gyre. The

base of surface mixed layer is defined as the depth at which the potential density difference exceeds 0.125 kg m^{-3} from the mean density in upper 10 m ⁴⁹. Below that, the halocline in the Canada Basin consists of the warm halocline layer and the cold halocline layer^{22,30}. The warm halocline layer is between the base of surface mixed layer and the first minimum in buoyancy frequency below the maximum value. Below this is the cold halocline, the base of which is determined using the ratio $R = \alpha \Delta T / \beta \Delta S$, where α is the thermal expansion coefficient and β is the haline contraction coefficient⁵⁰. In particular, the depth where $R = 0.05$, at which point the vertical density gradient is mainly due to the salinity gradient, as taken to be the base of cold halocline. The Atlantic water layer resides below this.

Freshwater content. The freshwater content is calculated as $\text{FWC}_1 = \int_h^0 \frac{(S_r - S(z))}{S_r} dz$, applied using the historical hydrographic data over the Beaufort Gyre region². The reference salinity S_r is 34.8 at the corresponding depth h , and $S(z)$ is the depth-dependent salinity. We also estimate the annual FWC using the DOT and GRACE data, following the methodology used in previous studies^{5,7,45}. As a simplification, the water column in the Beaufort Gyre can be considered as two homogeneous layers: a lighter layer with density $\rho_1 = 1022 \text{ kg m}^{-3}$ atop a denser layer with density $\rho_2 = 1028 \text{ kg m}^{-3}$. Variations in the freshwater content alter the thickness of the upper layer (Δh), which is reflected by the modulated DOT (η) and ocean mass (Δm). The freshwater content can thus be estimated by $\text{FWC}_2 = \frac{S_r - S_1}{S_r} A \sum_{i=0}^N \Delta h$, where $\Delta h = \eta \left(1 + \frac{\rho_1}{\rho_2 - \rho_1} \right) - \frac{\Delta m}{\rho_2 - \rho_1}$, A is the area of the Beaufort Gyre region, and N is the number of grid points. The ocean mass is estimated using the GRACE equivalent water thickness multiplied by the water density.

Data availability.

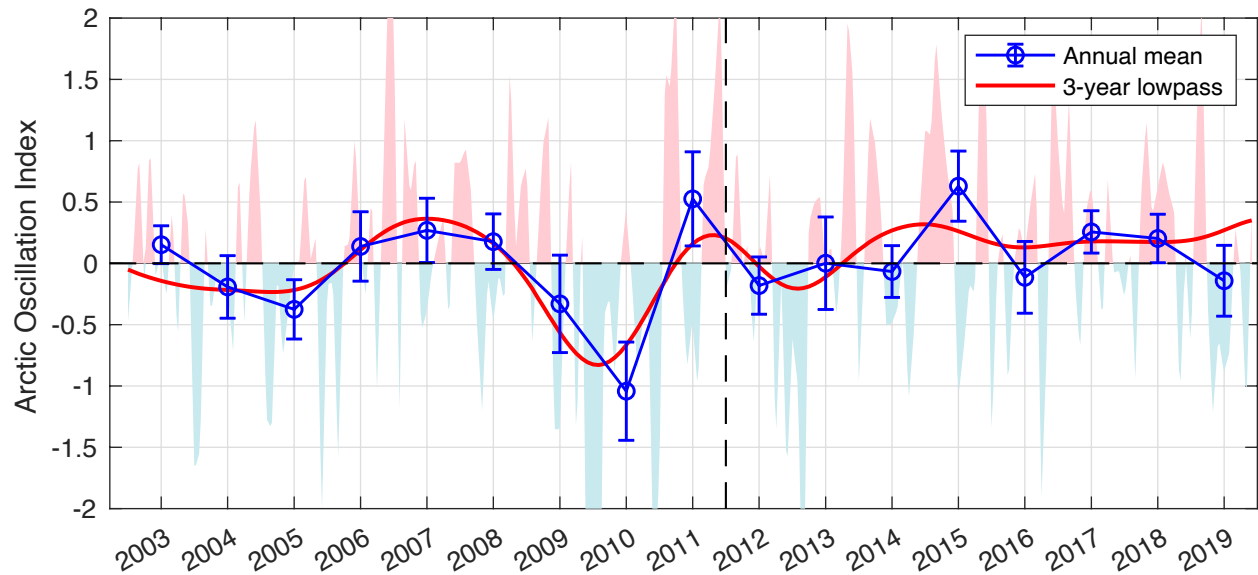
The historical hydrographic data are obtained from the following sources.

- (1) the Unified Database for Arctic and Subarctic Hydrography (UDASH, <https://doi.pangaea.de/10.1594/PANGAEA.872931>).
- (2) World Ocean Database 2018 (WOD18, <https://www.ncei.noaa.gov/products/world-ocean-database>).
- (3) Arctic Data Center (<https://arcticdata.io/catalog/data>)

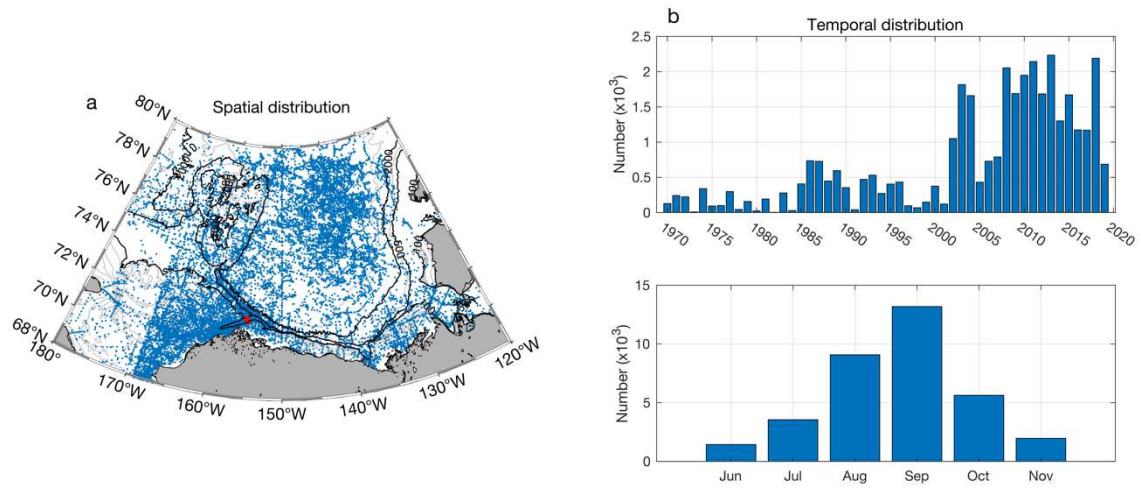
- (4) Beaufort Gyre Exploration Project (<https://www2.whoi.edu/site/beaufortgyre/data/data-overview/>)
- (5) Pacific Marine Environmental Laboratory (PMEL, <https://www.pmel.noaa.gov/epic/ewb/>);
- (6) NOAA Alaska Fisheries Science Center (<https://data.eol.ucar.edu/dataset/>);
- (7) University of Alaska Fairbanks Institute of Marine Science (UAFIMS, available at the Arctic Ocean Observing System, <http://www.aaos.org>);
- (8) Fisheries and Oceans Canada's Institute of Ocean Sciences (IOS, <https://www.pac.dfompo.gc.ca/science/index-eng.html>);
- (9) Japan Agency for Marine-Earth Science and Technology (JAMSTEC, <http://www.godac.jamstec.go.jp/darwin/e/>).
- (10) Korea Polar Data Center (<https://kpdccopen.kopri.re.kr>)

The dynamic ocean topography data produced by Armitage et al. (2016) can be found at http://www.cpom.ucl.ac.uk/dynamic_topography, and the updated dynamic ocean topography data from 2011-2019 is available at http://www.cpom.ucl.ac.uk/dynamic_topography/. GRACE data can be accessed via https://sealevel.nasa.gov/data/dataset/?identifier=SLCP_CSR-RL06-Mascons-v02_RL06_v02. The ERA5 reanalysis data are obtained from the European Center for Medium-Range Weather Forecasts (<https://rmets.onlinelibrary.wiley.com/doi/10.1002/qj.3803>). The GLORYS12 reanalysis is available at the Copernicus Marine and Environment Monitoring Service (<http://www.marine.copernicus.eu>). The JAMSTEC mooring data at the mouth of the Barrow Canyon from 2003-2019 are available at <https://www.jamstec.go.jp/iace/e/report/>. The monthly timeseries of Arctic Oscillation index is obtained from NOAA's Climate Prediction Center (https://www.cpc.ncep.noaa.gov/products/precip/CWlink/daily_ao_index/ao.shtml). The bathymetry data used in the study are from the International Bathymetric Chart of the Arctic Ocean (IBCAO) version 3 (https://www.gebco.net/about_us/committees_and_groups/scrum/ibcao/ibcao_v3.html).

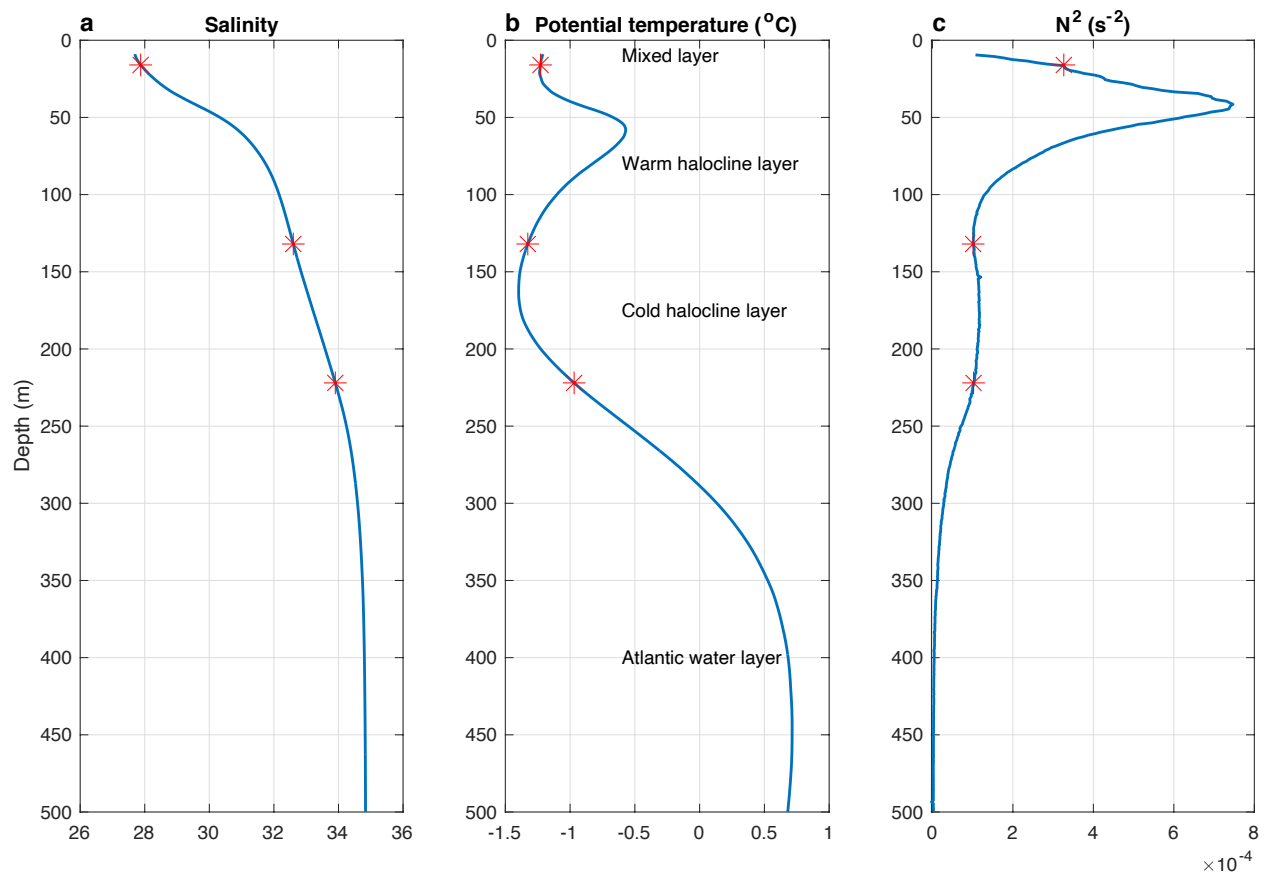
Extended Data



Extended Data Fig. 1 | Timeseries of the Arctic Oscillation Index. The shading denotes the monthly values; the annual averages are the blue symbols/curve, including the standard errors; the 3-year lowpassed timeseries is the red curve. The monthly timeseries is obtained from NOAA's Climate Prediction Center.



Extended Data Fig. 2 | Data coverage of the composite historical hydrographic dataset. a, Geographical map of the data distribution, and the Barrow Canyon mooring location (red dots). **b** The number of profiles in each year corresponding to the warm months and the monthly distribution.



Extended Data Fig. 3 | Vertical structure of water column in the Beaufort Gyre. Mean profiles of **a**, salinity, **b**, potential temperature (°C), and **c**, buoyancy frequency (N^2 , s⁻²) in the upper 500 m. The four layers partitioned by the red asterisks are: from the surface downward, the mixed layer, the warm halocline layer, the cold halocline layer, and the Atlantic water layer.

References

- 1 Proshutinsky, A., Krishfield, R. & Timmermans, M. L. Introduction to special collection on Arctic Ocean modeling and observational synthesis (FAMOS) 2: Beaufort Gyre phenomenon. *J. Geophys. Res. Oceans* **125**, e2019JC015400 (2020).
- 2 Proshutinsky, A. *et al.* Beaufort Gyre freshwater reservoir: State and variability from observations. *J. Geophys. Res. Oceans* **114** (2009).
- 3 Timmermans, M. L. & Marshall, J. Understanding Arctic Ocean circulation: A review of ocean dynamics in a changing climate. *J. Geophys. Res. Oceans* **125**, e2018JC014378 (2020).
- 4 Steele, M. *et al.* Circulation of summer Pacific halocline water in the Arctic Ocean. *J. Geophys. Res. Oceans* **109** (2004).
- 5 Proshutinsky, A. *et al.* Analysis of the Beaufort Gyre freshwater content in 2003–2018. *J. Geophys. Res. Oceans* **124**, 9658-9689 (2019).
- 6 Armitage, T. W. *et al.* Arctic Ocean surface geostrophic circulation 2003–2014. *The Cryosphere* **11**, 1767-1780 (2017).
- 7 Giles, K. A., Laxon, S. W., Ridout, A. L., Wingham, D. J. & Bacon, S. Western Arctic Ocean freshwater storage increased by wind-driven spin-up of the Beaufort Gyre. *Nature Geoscience* **5**, 194-197 (2012).
- 8 Zhong, W., Steele, M., Zhang, J. & Cole, S. T. Circulation of Pacific winter water in the Western Arctic Ocean. *J. Geophys. Res. Oceans* **124**, 863-881 (2019).
- 9 Regan, H. C., Lique, C. & Armitage, T. W. The Beaufort Gyre extent, shape, and location between 2003 and 2014 from satellite observations. *J. Geophys. Res. Oceans* **124**, 844-862 (2019).
- 10 Tsamados, M. *et al.* Impact of variable atmospheric and oceanic form drag on simulations of Arctic sea ice. *J. Phys. Oceanogr.* **44**, 1329-1353 (2014).
- 11 Yang, J. The Seasonal Variability of the Arctic Ocean Ekman Transport and Its Role in the Mixed Layer Heat and Salt Fluxes. *J. Clim.* **19**, 5366-5387 (2006).
- 12 Meneghello, G., Marshall, J., Timmermans, M.-L. & Scott, J. Observations of seasonal upwelling and downwelling in the Beaufort Sea mediated by sea ice. *J. Phys. Oceanogr.* **48**, 795-805 (2018).
- 13 Armitage, T. W., Manucharyan, G. E., Petty, A. A., Kwok, R. & Thompson, A. F. Enhanced eddy activity in the Beaufort Gyre in response to sea ice loss. *Nature Communications* **11**, 1-8 (2020).
- 14 Manucharyan, G. E. & Spall, M. A. Wind-driven freshwater buildup and release in the Beaufort Gyre constrained by mesoscale eddies. *Geophys. Res. Lett.* **43**, 273-282, doi:10.1002/2015gl065957 (2016).
- 15 Meneghello, G., Marshall, J., Cole, S. T. & Timmermans, M. L. Observational inferences of lateral eddy diffusivity in the halocline of the Beaufort Gyre. *Geophys. Res. Lett.* **44**, 331-312,338 (2017).
- 16 Regan, H., Lique, C., Talandier, C. & Meneghello, G. Response of total and eddy kinetic energy to the recent spinup of the Beaufort Gyre. *J. Phys. Oceanogr.* **50**, 575-594 (2020).
- 17 Zhang, J. *et al.* The Beaufort Gyre intensification and stabilization: A model-observation synthesis. *J. Geophys. Res. Oceans* **121**, 7933-7952 (2016).

- 18 Itoh, M., Nishino, S., Kawaguchi, Y. & Kikuchi, T. Barrow Canyon volume, heat, and freshwater fluxes revealed by long-term mooring observations between 2000 and 2008. *J. Geophys. Res. Oceans* **118**, 4363-4379 (2013).
- 19 Foukal, N. P., Pickart, R. S., Moore, G. & Lin, P. Shelfbreak downwelling in the Alaskan Beaufort Sea. *J. Geophys. Res. Oceans* **124**, 7201-7225 (2019).
- 20 Lin, P., Pickart, R. S., Moore, G., Spall, M. A. & Hu, J. Characteristics and dynamics of wind-driven upwelling in the Alaskan Beaufort Sea based on six years of mooring data. *Deep Sea Res. II* **162**, 79-92 (2019).
- 21 Lin, P., Pickart, R. S., Våge, K. & Li, J. Fate of warm Pacific water in the Arctic basin. *Geophys. Res. Lett.* **48**, e2021GL094693 (2021).
- 22 Timmermans, M. L., Marshall, J., Proshutinsky, A. & Scott, J. Seasonally derived components of the Canada Basin halocline. *Geophys. Res. Lett.* **44**, 5008-5015 (2017).
- 23 Krishfield, R. A. *et al.* Deterioration of perennial sea ice in the Beaufort Gyre from 2003 to 2012 and its impact on the oceanic freshwater cycle. *J. Geophys. Res. Oceans* **119**, 1271-1305 (2014).
- 24 Haine, T. W. *et al.* Arctic freshwater export: Status, mechanisms, and prospects. *Global and Planetary Change* **125**, 13-35 (2015).
- 25 Tsubouchi, T. *et al.* The Arctic Ocean seasonal cycles of heat and freshwater fluxes: Observation-based inverse estimates. *J. Phys. Oceanogr.* **48**, 2029-2055 (2018).
- 26 Zhang, J. *et al.* Labrador Sea freshening linked to Beaufort Gyre freshwater release. *Nature communications* **12**, 1-8 (2021).
- 27 Gelderloos, R., Straneo, F. & Katsman, C. A. Mechanisms behind the temporary shutdown of deep convection in the Labrador Sea: Lessons from the Great Salinity Anomaly years 1968–71. *J. Clim.* **25**, 6743-6755 (2012).
- 28 Itoh, M. *et al.* Interannual variability of Pacific Winter Water inflow through Barrow Canyon from 2000 to 2006. *J. Oceanogr.* **68**, 575-592 (2012).
- 29 Lin, P. *et al.* On the nature of wind-forced upwelling and downwelling in Mackenzie Canyon, Beaufort Sea. *Prog. Oceanogr.* **198**, 102674 (2021).
- 30 Woodgate, R. A., Aagaard, K. & Weingartner, T. J. Monthly temperature, salinity, and transport variability of the Bering Strait through flow. *Geophys. Res. Lett.* **32**, doi:10.1029/2004gl021880 (2005).
- 31 Woodgate, R. A. & Peralta-Ferriz, C. Warming and Freshening of the Pacific Inflow to the Arctic from 1990–2019 implying dramatic shoaling in Pacific Winter Water ventilation of the Arctic water column. *Geophys. Res. Lett.* **48**, e2021GL092528 (2021).
- 32 Woodgate, R. A. Increases in the Pacific inflow to the Arctic from 1990 to 2015, and insights into seasonal trends and driving mechanisms from year-round Bering Strait mooring data. *Prog. Oceanogr.* **160**, 124-154 (2018).
- 33 Pacini, A. *et al.* Characteristics and transformation of Pacific winter water on the Chukchi Sea shelf in late spring. *J. Geophys. Res. Oceans* **124**, 7153-7177 (2019).
- 34 Pickart, R. S. *et al.* Circulation of winter water on the Chukchi shelf in early Summer. *Deep Sea Res. II* **130**, 56-75 (2016).
- 35 Lin, P. *et al.* Circulation in the vicinity of Mackenzie Canyon from a year-long mooring array. *Prog. Oceanogr.* **187**, 102396 (2020).

- 36 Nikolopoulos, A. *et al.* The western Arctic boundary current at 152°W: Structure, variability, and transport. *Deep Sea Research II* **56**, 1164-1181, doi:10.1016/j.dsr2.2008.10.014 (2009).
- 37 Jean-Michel, L. *et al.* The Copernicus global 1/12° oceanic and sea ice GLORYS12 reanalysis. *Frontiers in Earth Science* **9**, 585 (2021).
- 38 Corlett, W. B. & Pickart, R. S. The Chukchi slope current. *Prog. Oceanogr.* **153**, 50-65 (2017).
- 39 Leng, H., Spall, M. A., Pickart, R. S., Lin, P. & Bai, X. Origin and Fate of the Chukchi Slope Current Using a Numerical Model and In-situ Data. *J. Geophys. Res. Oceans*, e2021JC017291 (2021).
- 40 Li, M. *et al.* Circulation of the Chukchi Sea shelfbreak and slope from moored timeseries. *Prog. Oceanogr.*, doi:10.1016/j.pocean.2019.01.002 (2019).
- 41 Mallett, R. *et al.* Record winter winds in 2020/21 drove exceptional Arctic sea ice transport. *Communications Earth & Environment* **2**, 1-6 (2021).
- 42 Behrendt, A., Sumata, H., Rabe, B. & Schauer, U. UDASH—Unified Database for Arctic and Subarctic Hydrography. *Earth System Science Data* **10**, 1119-1138 (2018).
- 43 Danielson, S. *et al.* Manifestation and consequences of warming and altered heat fluxes over the Bering and Chukchi Sea continental shelves. *Deep Sea Res. II* **177**, 104781 (2020).
- 44 Smith, W. & Wessel, P. Gridding with continuous curvature splines in tension. *Geophysics* **55**, 293-305 (1990).
- 45 Armitage, T. W. *et al.* Arctic sea surface height variability and change from satellite radar altimetry and GRACE, 2003–2014. *J. Geophys. Res. Oceans* **121**, 4303-4322 (2016).
- 46 Hersbach, H. *Operational global reanalysis: progress, future directions and synergies with NWP*. (European Centre for Medium Range Weather Forecasts, 2018).
- 47 Stabeno, P. J. & McCabe, R. M. Vertical structure and temporal variability of currents over the Chukchi Sea continental slope. *Deep Sea Res. II* **177**, 104805 (2020).
- 48 Save, H., Sun, A. Y., Scanlon, B. R. & Rateb, A. in *AGU Fall Meeting Abstracts*. G001-001.
- 49 Marshall, J. & Radko, T. Residual-mean solutions for the Antarctic Circumpolar Current and its associated overturning circulation. *J. Phys. Oceanogr.* **33**, 2341-2354 (2003).
- 50 Bourgain, P. & Gascard, J.-C. The Arctic Ocean halocline and its interannual variability from 1997 to 2008. *Deep Sea Res. I* **58**, 745-756 (2011).